

Cooperation and competing of antipolar charge order and superconducting states in a quasi-2D superatomic metallic crystal

Shuya Xing^{1,4,5,+,*}, Zhongxu Wei^{2,+}, Xu Chen^{2,*}, Junming Zhang², Zhenyu Yuan², Jiali Zhao², Feng Jin², Tao Sun², Huifen Ren², Minjie Cui², Hong Chang^{1,4,5}, Tianping Ying², Jiangang Guo², Xiaolong Chen², Shifeng Zhao^{1,4,5}, Wenping Zhou^{1,4,5}, Xinqi Li^{1,4}, Tian Qian², and Zhihai Cheng^{3,*}

¹*Research Center for Quantum Physics and Technologies, Inner Mongolia University, Hohhot 010021, China*

²*Beijing National Laboratory for Condensed Matter Physics, Institute of Physics, Chinese Academy of Sciences, Beijing 100190, China*

³*Beijing Key Laboratory of Optoelectronic Functional Materials & Micro-nano Devices, Department of Physics, Renmin University of China, Beijing 100872, China*

⁴*School of Physical Science and Technology, Inner Mongolia University, Hohhot 010021, China*

⁵*Inner Mongolia Key Laboratory of Microscale Physics and Atom Innovation, Inner Mongolia University, Hohhot 010021, China*

Exploring various unexpected new quantum states and their corresponding extraordinary physics in low dimensional quantum materials, and investing them into application fields, is a primary concern of condensed matter physics. Previously, we performed joint experiments and theoretical calculations to investigate a superatomic crystal of $\text{Au}_6\text{Te}_{12}\text{Se}_8$ with low symmetry, which stacks through non-covalent inter-cube quasi-bonds. $\text{Au}_6\text{Te}_{12}\text{Se}_8$ exhibits a triple-cube charge density wave and spatially polarized metallic states interweaving at 9 K. In addition, it undergoes a BKT phase transition at 2.8 K to form a quasi-two-dimensional superconducting state. The subsequent high-pressure experimental results indicate that the two quantum states above compete with superconductivity. Here, we experimentally revealed competition and coexistence among superconductivity, triple-cube charge density waves, and polarized metallic states during further temperature-decreasing process, as examined using ultra-low temperature scanning tunneling microscopy/spectroscopy, transport measurement, and Raman spectra. An extraordinary inversion symmetry broken emerged inside the triple-cube-period of the original CDW at 300 mK, leading to the polarized metallic states transforming into parallel polarization states. The evidence of spontaneous polarization coexisting with superconductivity in real space is extremely rare and has been revealed by STM. In addition, transport and Raman measurements indicate that there are multiple phase transition temperatures from 80 K to that below the superconducting transition temperature of $\text{Au}_6\text{Te}_{12}\text{Se}_8$, which may also contain more unknown exotic quantum states, providing a platform for further exploration of intriguing physical properties.

⁺ These authors contributed equally: Shuya Xing and Zhongxu Wei

* Email: 111992026@imu.edu.cn xchen@iphy.ac.cn zhihaicheng@ruc.edu.cn

I. INTRODUCTION

In low dimensional quantum materials, the coexisting and competing of multiple orders, contain rich physical meanings. Exploring this aspect is a hot topic in developing condensed matter physics. Fundamentally new and unexpected quantum states emerge, e.g. Pair density waves [1] intertwined with chiral flux phase [2] in vanadium-based Kagome metals, AV_3Sb_5 ($A = K, Rb$ or Cs), Magnetic-field-sensitive charge density waves [3] coexist with chiral spin-triplet superconductivity [4] in heavy-fermion superconductor UTe_2 , as well as multipolar order phase in multipole-induced superconductor material $PrTi_2Al_{20}$ [5] and among the others. These unusual electronic structures can be investigated and utilized to achieve extraordinary physical properties.

Special crystal structures have a profound impact on electronic, spin, and orbital behavior, such as the Kagome lattice structure: which exhibits strong two-dimensional characteristics in electronic spectra, transport properties [6], and other aspects due to its special symmetry constraints. Make it have a series of extraordinary electronic structures such as flat bands, Dirac points [7], and Van Hoff singularities [8]. A prominent feature is the time-reversal symmetry breaking caused by the non-magnetic environment in the Kagome lattice, also known as the chiral flux phase (CFP) [2]. Lacking inversion or time-reversal symmetry will profoundly modify the properties of the superconducting phases [9, 10] and charge density waves [11]. The primary features include chiral charge density waves [12], chiral superconductivity [4], spontaneous polarization [13], singlet-triplet mixing of cooper-pair states [14], and topological superconductivity [15], etc, which has attracted much interest.

Inversion-symmetry breaking typically emerges only in a limited classification of non-centrosymmetric or local symmetry-breaking crystal structures [10, 16]. Some localized methods, such as electron injection [17], molecular adsorption [18], or the construction of mirror twin boundaries [19] can realize chiral characteristics. However, it is difficult to create more dimensions and degrees of freedom in traditional crystal structures to achieve more complex and exotic quantum states. Fabricating superatomic crystals is an effective way to break through this bottleneck. By artificially designing and manufacturing pure inorganic superatomic crystals, multiple levels of symmetry breaking within and between superatoms can be achieved, leading to the development of richer quantum phases. So far, superconductivity [20], magnetism [21], ferroelectricity [22], charge density waves [23], etc, have all been successfully materialized in inorganic superatomic crystals.

Nonetheless, the relatively weak bonding between superatoms cannot be ignored as an obstacle to the formation of quantum states. The clue is to find superatomic interactions that combine strong stability, a small energy gap, and flexible controllable superatomic interactions. Recently, an artificially synthesized superatomic crystal, $Au_6Te_{12}Se_8$ (ATS), exhibited various exotic quantum states, such as two-dimensional superconductivity [24], antipolar metallic states, and superatomic periodic charge density waves (TCCDW), which have sparked a lot of attention [23]. Subsequent

studies have shown that the interwoven TCCDW and antipolar metallic states gradually break the translational and center inversion symmetry as the temperature decreases, and compete with superconductivity, suggesting their participation in superconducting pairing and candidate for unconventional superconductivity [25].

Here we experimentally demonstrate the coexistence and competition between TCCDW, antipolar metallic states, and superconductivity in ATS during a further temperature-decreasing process. The corresponding electrical properties and surface electronic structures of ATS were revealed using an ultra-low-temperature scanning tunneling microscope (ULT-STM, 300mK) together with transport and Raman measurements. At 300mK, we observed an extraordinary inversion symmetry broken inside the triple-cube-period of the TCCDW along the a -axis, which led to the antipolar metallic states at 9K to transform into parallel polarization orders. A “U-shaped” superconducting gap with a half-width of ~ 1.5 meV was distinguished by the differential conductance (dI/dV) spectra, indicating that the superconductivity of ATS originates from super-strong electron-electron correlation. In addition, magnetic susceptibility and Raman measurements show anomalous magnetic responses at ~ 50 K, suggesting the presence of more unexpected quantum states in the system. These exotic quantum states, along with superconducting cooper pairing mechanisms in ATS, require further exploration.

II. Results

A. Superatomic crystal structure and physical properties of ATS

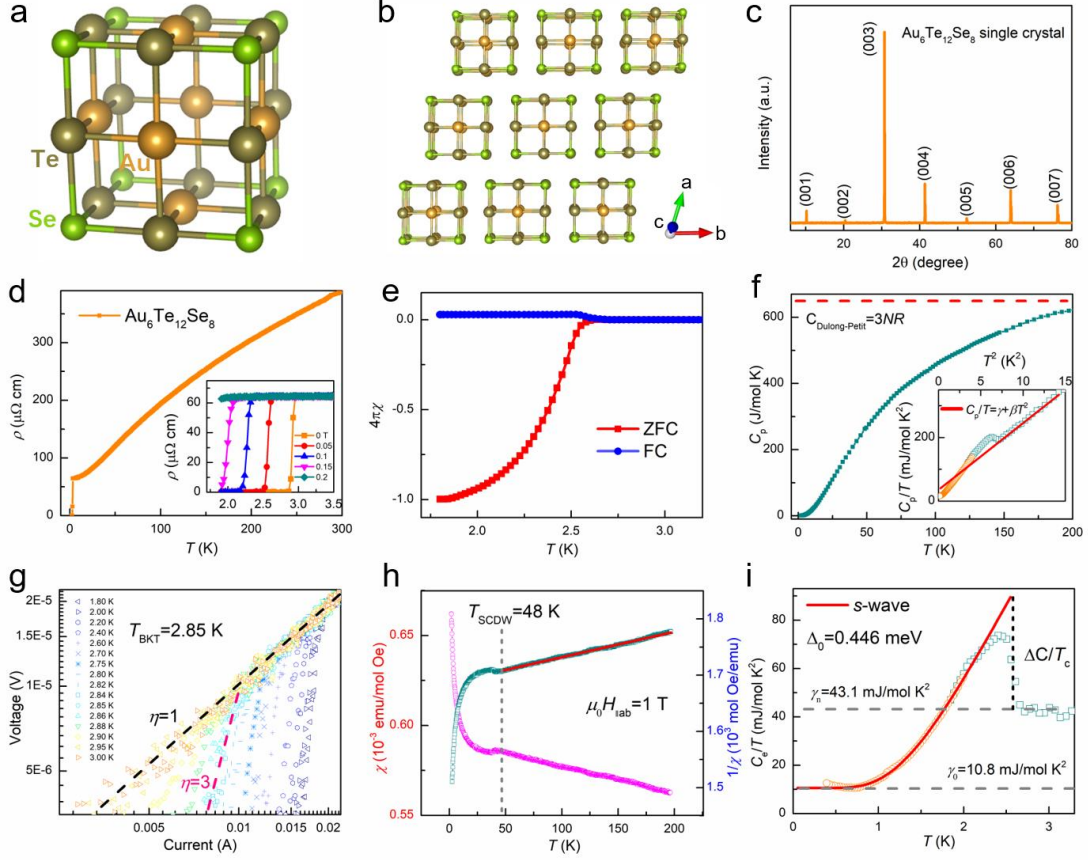


Figure 1. Crystal structure, XRD patterns, and physical properties of $\text{Au}_6\text{Te}_{12}\text{Se}_8$ (ATS). (a) The structure of a single cube of ATS is regarded as a superatom (0D). Au, Te, and Se atoms are represented by golden, brown, and green balls, respectively. (b) 3D crystal structure of ATS in the ab -plane. (c) powder X-ray diffraction (XRD) pattern of ATS single crystal. (d) Electrical resistivity of ATS from 1.8 to 300 K. The inset shows the electrical resistivity under different magnetic fields. (e) Superconducting volume fractions of ATS under $H = 10$ Oe. (f) Heat capacity (C_p) of ATS as a function of temperature, The red dashed line represents the Dulong–Petit limit. The inset shows C_p/T versus T^2 , in which the red straight line represents the fit with the formula $C_p/T = \gamma + \beta T^2$ for the normal-state data. (g) V – I curves of ATS plotted in a log-log scale at various temperatures near T_c . Dash lines denote the fitting result with $V \sim I^\eta$ scaling law, the $\eta = 1$ (black) and 3 (red) curves, respectively. (h) Temperature dependence of magnetic susceptibility χ and $1/\chi$ of ATS with the magnetic field parallel to the ab plane. The red lines denote the Curie–Weiss fit. (i) Electronic specific heat divided by temperature C_e/T of ATS in the superconducting state, where $C_e = C - \beta T^3$, and the red line is the theoretical curves calculated as the BCS model.

Figure 1(a)-(b) shows the crystal structure of the all-inorganic superatomic $\text{Au}_6\text{Te}_{12}\text{Se}_8$ (ATS), which consists of rigid cubic blocks with an identical chemical composition of six Au, twelve Te, and eight Se atoms. These cubes are stacked in the

ab plane direction via non-covalent inter-cube quasi-bonds to form a quasi-2D superatomic crystal. The single crystals of ATS were grown by the self-flux method. Figure 1(c) shows the powder X-ray diffraction pattern of ATS single crystal. Only (00 l) Bragg peaks show up, demonstrating that the largest surface is *ab*-plane. The peaks are sharp and well-defined, indicating good crystallized quality of the ATS crystal. The atomic ratio of Au: Te: Se is 21.49: 49.68: 28.84 within the measurement precision ($\pm 3\%$ depending on the elements) as the EDS pattern in Fig. S1, consistent with the atomic ratio of the initial stoichiometric $\text{Au}_6\text{Te}_{12}\text{Se}_8$.

Figure 1(d) shows the temperature dependence of the ρ - T curves for good crystallized quality ATS single crystal at zero field. The ρ decreases upon cooling, exhibiting a character of good metal. The T_c defined by $\rho = 0$ is near 2.8 K, which is consistent with our previous works. From the bottom inset of Figure 1(d), the low-temperature resistivity of the ATS single crystal was measured in magnetic fields up to 0.2 T. With increasing magnetic field, the T_c decreases at the rate of ~ 0.5 K/kOe, confirming the good superconductivity of the sample. Figure 1(g) shows the V - I curves near the critical current at around T_c , in which the critical I_c increases as the temperature decreases and finally reaches 15 mA at 1.8 K. The exponent, η , from power law $V \sim I^\eta$ increases from 1 (ohmic law) to 3 and more with temperature decreasing. The η reaches 3 at $T_{\text{BKT}} = 2.85$ K, which is the signature of the Berezinskii-Kosterlitz-Thouless (BKT) transition. Figure 1(e) plots the temperature-dependent χ of ATS in zero-field cooling (ZFC) and field-cooling (FC) modes under 10 Oe. The pronounced diamagnetic signals are exhibited below 2.78 K. The superconducting volume fraction is estimated to be 100% at 1.8 K, confirming the bulk superconductivity. Figure 1(h) shows temperature-dependent magnetization measurements performed with the magnetic field perpendicular to the *c*-axis on single crystal ATS under a 1 T field. Cusp-like anomalies at around 48 K coincide with our previous resistivity conductivity measurement of the ATS flake sample [23, 25], implying a novel magnetic response (T_{SCDW}), similar to the character in CsV_3Sb_5 and CsCr_3Sb_5 [6, 26]. The $\chi(T)$ curve at high temperatures can be fitted by the Curie-Weiss behavior (see Figure 1(h)). We thus fitted the data with the Curie-Weiss law, $\chi(T) = \chi_0 + C/(T + \theta)$, where C refers to the Curie constant and θ is paramagnetic Curie-Weiss temperature. The Curie constant corresponds to effective magnetic moments of about $0.37 \mu_B$ /per atom, suggesting the existence of local moment.

We measured the specific heat (C_p) of ATS from 0.4 K to 200 K, which is plotted in Figure 1(f). Notably, no significant phase transition was observed 10-200 K, this phenomenon is common in some systems with the CDW-like transition [27, 28]. The inset of Figure 1(f) shows the plot of C_p/T versus T^2 . The bulk SC of ATS is confirmed by a large superconducting jump at ~ 2.6 K in the specific heat, by the both resistivity

conductivity and magnetic susceptibility data presented above. In the normal state, the C_p curve is well fitted by $C_p/T = \gamma + \beta T^2$ from 3–10 K, where the first and the second terms correspond to the normal-state electronic and phonon contribution, respectively. Furthermore, we obtain Sommerfeld coefficient $\gamma = 43.1 \text{ mJ mol}^{-1} \text{ K}^2$ and $\beta = 20.7 \text{ mJ mol}^{-1} \text{ K}^4$. Extrapolating the data to 0 K leads to a residual $\gamma_0 = 10.8 \text{ mJ mol}^{-1} \text{ K}^2$, indicating a contribution by a non-superconducting phase in volume of about 25%. Thus we obtain the superconducting γ_s as $32.3 \text{ mJ mol}^{-1} \text{ K}^2$, which results in the dimensionless jump value of $\Delta C_e/\gamma_s T_c$ of 1.45, see Figure 1(i). This value is consistent with the Bardeen–Cooper–Schrieffer (BCS) value (1.43) for superconductors in the weak coupling limit. The C_e/T data can be fitted by the expression from the BCS theory, $C_e/T \propto e^{-\Delta/k_B T}$. The yielding superconducting gap $\Delta(0) = 0.446 \text{ meV} = 5.14 k_B \text{ K}$. The good agreement between the measured data and the BCS fitting provides evidence for an s -wave isotropic superconducting gap. Furthermore, the fitting yields $2\Delta(0)/k_B T_c = 3.95$, which is larger than the value of 3.52 for the BCS weak coupling limit.

B. Electronic structure of ATS at liquid helium temperature

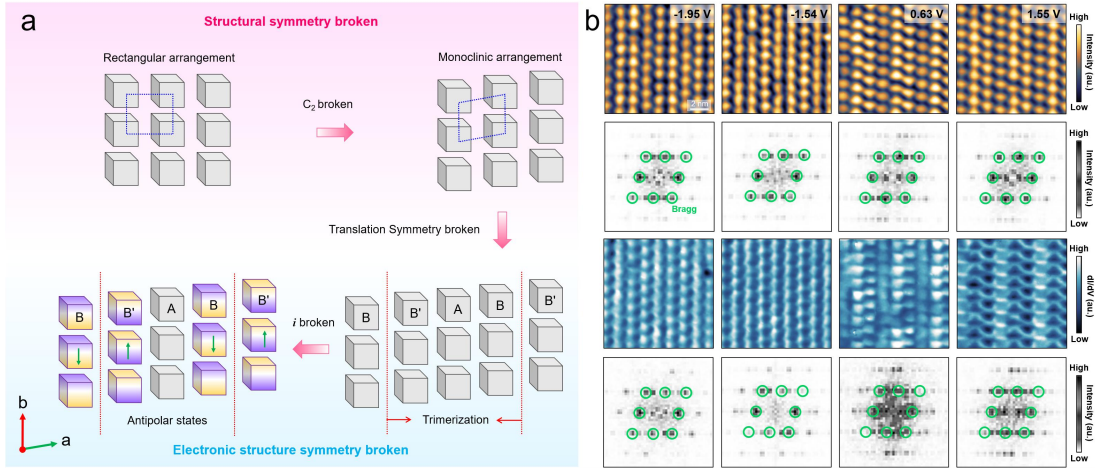


Fig. 2. Temperature decreasing suppresses the triple-cube-period CDW, before the superconductivity takes place in ATS (the real space electronic structure of ATS at 4.6 K, $T_{SC}=2.8$ K). (a) The schematic of TCCDW and antipolar metallic states formation in ATS sequentially breaks translational symmetry along the a -axis and intra-cube central inversion symmetry on the b -axis. (b) The first row of the images are topographies of ATS obtained at liquid helium temperature (4.6 K). The third row is the dI/dV mappings performed *in-situ* (local density of state, LDOS). The second and fourth rows are the corresponding fast Fourier transform (FFT) patterns of the topographies and dI/dV mappings. The green circles mark the Bravais vectors of the pristine a - b plane layer, respectively, and the points outside the green circles correspond to the characteristics of the triple-cube-period CDW.

Figure 2(a) shows the scheme of the two interweaved charge orders in the layered ATS super-atomic crystal, which are formed by the sequential symmetry-

reducing process in the geometric and electronic structure. The high-symmetric stacking of superatomic building blocks forms a square arrangement. The square arrangement is reduced to a monoclinic arrangement by breaking of C_2 symmetry to achieve the minimum directive inter-cube interaction energy. The inter-cube electronic energy is minimized by losing the translation symmetry of monoclinic arrangement (PI symmetry), resulting in the trimerization of superatomic chains along the a -axis (triple-cube CDW, TCCDW). The trimerization of cubes further breaks the intra-cube inversion symmetry of B (and B'), resulting in the emergence of superatomic polarization along the b -axis, and reducing the electron energy. The interweaved TCCDW and antipolar electronic states substantially originate from low-symmetric geometry structure (monoclinic arrangement) in ATS. According to the previous work [23], STM topography performed at 9K shows distinctly “up-triangular” (UT), “olive” (O), and “down-triangular” (DT) shapes in the occupied state, as well as “down-triangular” (UT), “rhombus” (O), and “up-triangular” (DT) shapes in the unoccupied state, which are manifestations of two interweaved charge orders in real space.

To investigate the evolution of ATS electronic structure with temperature decreasing, STM topographies and dI/dV mappings are performed at liquid helium temperature (4.6 K), as shown in Figure 2(b). Compared to the state at 9K, the appearance of CDW gets blurry, and the corresponding characteristics are also weakened in fast Fourier transform (FFT). As shown in the dI/dV mappings, the difference between the occupied state and the empty state is tremendous: in the occupied state, the local density of states exhibits a uniform chain-like feature along the b -axis. While in the unoccupied state, the trimerization of the electronic density of states among superatoms is more pronounced. It is noticed that -1.54V and 1.55V correspond to the inter-cube states, while -1.95V and 0.63V correspond to the intra-cube states (as shown in Fig. S2). However, the LDOS of the occupied state at 9K strictly corresponds to the intra-cube states of the superatom, while the unoccupied state corresponds to the inter-cube states (Fig. S3). With the temperature decreasing, the energy level of superatomic molecular orbitals (bonding and antibonding states) partially shifts.

C. Electronic structure of ATS at 300mK

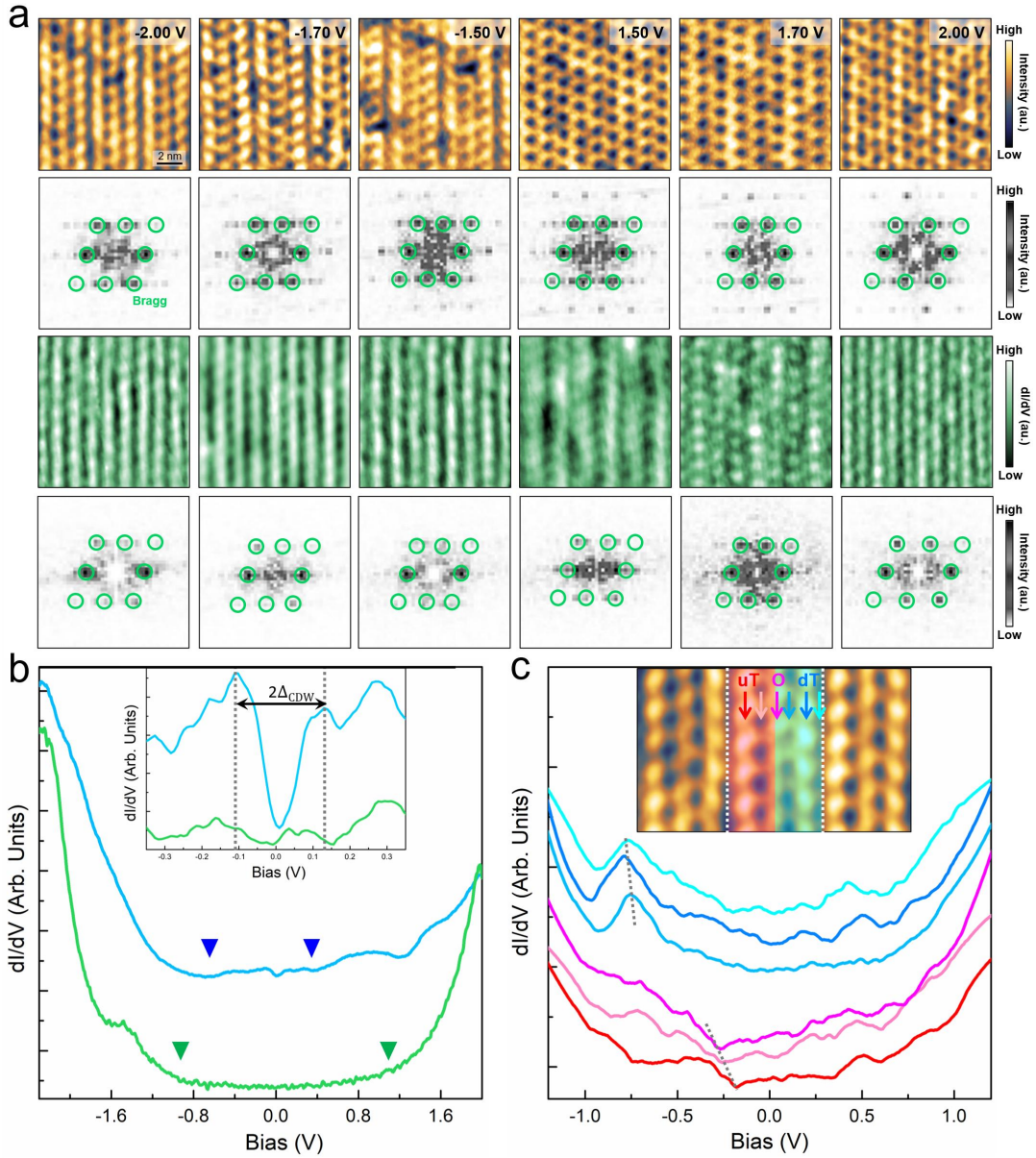


Fig.3. After superconductivity occurs, the triple-cube-period CDW is further suppressed (real space electronic structure of ATS at 300 mK). (a) The first row of the images are topographies of ATS performed at 300 mK, and the third row is the dI/dV mappings obtained *in-situ*. There is a significant difference in topographies between the occupied state and the unoccupied state. The second and fourth rows are the corresponding fast Fourier transform (FFT) patterns of the topographies and dI/dV mappings. The green circles in the FFT indicate the Bravais vectors of the a - b plane. The characteristics of the triple-cube-period CDW are suppressed completely in the FFT of dI/dV mappings. (b) Comparison of the differential conductance (dI/dV) spectra of ATS at 4.6 K and 300 mK, respectively. (where the blue line corresponds to 4K and the green line corresponds to 300 mK). The arrows mark the location of the energy gap, which significantly increases from 4.6 K to 300 mK. The insert above shows the short range of STS near the Fermi level, where the 4.6 K STS exhibits a CDW gap of approximately 0.12 eV. (c) STS spectra

on/between the UT, O, and DT cube units within the triple-cube-period at 300 mK. They were categorized into two groups (marked in red and blue, respectively) according to their different characteristics, indicating that the central inversion symmetry of UT and DT chains concerning O is broken.

The superconducting transition temperature of ATS is $T_c=2.8$ K, and the electronic structure of ATS has been performed by STM before entering the superconducting state (Figure 2). TCCDW and antipolar metallic states are slightly suppressed at liquid helium temperature. Figure 3(a) shows topographies and dI/dV mappings of ATS at 300 mK, which is presently superconducting. The antipolar metallic states are difficult to distinguish in topographies, while the TCCDW is preserved in the occupied state but almost disappears in the unoccupied state. In the corresponding dI/dV mappings, the suppression effect on charge orders is more significant as temperature decreases: $-2V$ corresponds to the inter-cube states, while -1.7 V, $-1.5V$, $1.7V$ and $2V$ corresponds to the intra-cube states, through comparing topographies with dI/dV mappings *in-situ* (as shown in Fig. S4). The characteristics of charge orders almost disappeared completely in the FFT of dI/dV mapping.

Figure 3(b) shows the differential conductance (dI/dV) spectra performed before and after superconductivity takes place. All of these spectra show large energy gaps similar to molecules. At 4.6 K, the molecular-like energy gap is about 1.0 eV (in blue), and after decreasing to 300 mK, the energy gap of the gap enlarges to 2.0 eV (in green). After narrowing the energy window to ± 0.35 eV, there's a quasigap of approximately 0.11 eV around the Fermi level at 4.6 K, which is slightly smaller than that at 9 K [23]. The density of states at 300 mK is not incompletely suppressed.

Figure 3(c) is the chain- and interchain-specific differential conductance (dI/dV) spectra obtained on/between the UT, O, and DT chains at 300 mK. The spectra are categorized into two groups: the first group shows a dip (red) around $-0.25V$, and the second group shows a peak (blue) near $-0.75V$. Most of these spectra have weak characteristic peaks at $0.3V$ and $0.5V$, respectively. The difference among the spectra in the occupied state indicates that within the triple-cube-period CDW, the central inversion symmetry between the UT chain and the DT chain was further broken, forming a new periodic modulation of electronic structures in real space.

D. Parallel arrangement of polarized metallic states and superconductivity

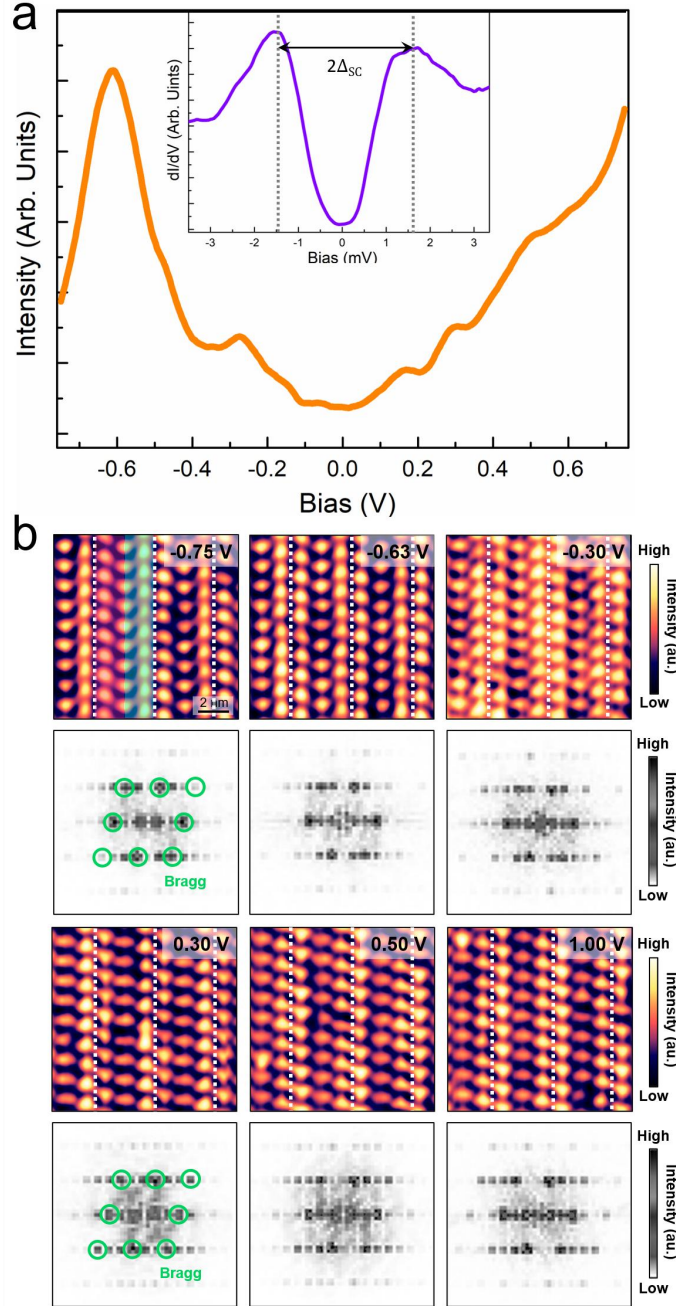


Fig. 4. In-gap states and superconductivity at 300 mK. (a) The differential conductance (dI/dV) spectra of ATS performed at a short range of $\pm 0.75\text{V}$ (in orange). Several well-defined characteristics of in-gap states were clearly visualized at the bias of -0.63V , -0.30V , 0.30V , and 0.5V . Further reducing the energy window to mV magnitude, a "U"-shaped superconducting gap of approximately 0.12 eV was obtained (as shown in the purple curve inserted above). (b) STM topographies and corresponding FFT patterns were obtained around the in-gap states corresponding to Fig. 4(a). The white dashed line marks the triple-cube-period. In the occupied state, the central inversion symmetry among the superatomic chains is further broken, which corresponds to Fig. 3 (c).

Below the superconducting transition temperature of ATS, the CDW gap around the Fermi level is completely suppressed. As shown in Figure 4(a), some in-gap states can be distinguished in the reduced range differential conductivity spectrum at 300mK, with peak energy positions corresponding to -0.63V, -0.3V, 0.3V, and 0.5V. The energy positions of these peaks, however, generally correspond to the characteristic electronic structure in Figure 3(c), the slight shift only originating from the heterogeneity where the spectrum is performed. When the energy window is reduced to ± 3 mV, a "U-shaped" superconducting gap (SC gap) of ATS can be clearly distinguished (insert of Figure 4(a)). The differential conductivity spectrum reveals completely vanished DOS near the Fermi level. Compared to a single BCS-type isotropic s-wave gap, the coherence peaks exhibited in the SC gap of ATS are not sharp enough [20, 29]. Half the distance between the two coherence peaks (Δ) is estimated to be ~ 1.5 meV. According to $\Delta/(k_B \times T_c) \sim 1.76$ is a BCS system, substituting the relevant values: $\Delta = 1.5$ meV and $T_c = 2.8$ K. The calculated result is 6.22, which is much higher than 1.76, indicating that ATS is a super-strong electron correlation system [30].

The significance of the in-gap states is revealed *in-situ* as shown in Figure 4(b). TCCDW is clearly resolved in STM topography at each bias voltage, which breaks the translational symmetry of inter-cube Te-Te bonding along the *a*-axis. The polarization of superatoms shows a triangle-shaped electronic state, which originates from the inversion symmetry breaking inside the superatoms along the *b*-axis. However, the polarized states in the anti-parallel arrangement at 9K are broken in the occupied state, while they are well preserved in the unoccupied state. In the occupied state, both UT and DT chains exhibit "up-triangular" shapes with parallel polarization directions, which is consistent with the result of central symmetry breaking between UT and DT chains within a triple-cube-period CDW mentioned in Figure 3(c). The anti-parallel locking effect of the TCCDW on polarization has been eliminated within this energy scale. The parallel polarization arrangement is particularly obvious at -0.75V and -0.3V, which are consistent with the electronic density of state characteristics corresponding to the blue and red regions in Figure 3(c). The above description demonstrated that superconducting states and TCCDW can coexist in ATS. However, superconductivity causes a certain degree of damage to the antipolar metallic states, resulting in the emergence of parallel polarized states.

E. Temperature-dependent Raman measurements before and after superconductivity

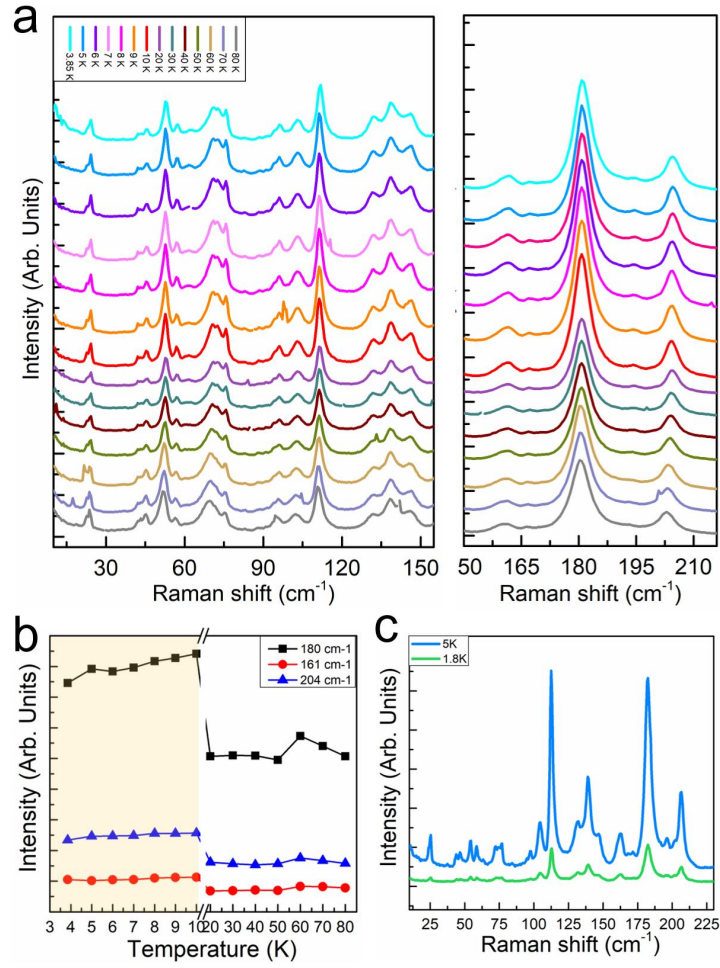


Fig. 5. Temperature-dependent Raman spectrum. (a) The temperature-dependent Raman shift (TDRS) of ATS from 80 K to 3.85 K. The left part of the image shows the Raman shift range from 10 cm⁻¹ to 155 cm⁻¹, while the right part shows the range around 180 cm⁻¹. (b) The temperature-dependent Raman intensity at 180 cm⁻¹ with its two secondary peaks (at 161 cm⁻¹ and 204 cm⁻¹). The orange-shaded area marked the suppressive effect of temperature decreasing on Raman intensity. (c) Comparison of Raman shifts before (5 K, in blue) and after (1.8 K, in green) superconductivity.

The evolution process of the triple-cube-period CDW from 80 K to 1.8 K was also demonstrated by our temperature-dependent Raman shift (TDRS) measurements as the temperature decreased (Figure 5). Six main TDRS peaks are located at 24 cm⁻¹, 53 cm⁻¹, 71 cm⁻¹, 112 cm⁻¹, 139 cm⁻¹, and 181 cm⁻¹, respectively (Figure 5(a)). Except for 24 cm⁻¹ and 71 cm⁻¹, any other main vibration peak is accompanied by two secondary vibration peaks, appearing in groups of three. These secondary vibration peaks are probably related to certain collective vibration modes with triple-cube-periods. Among them, the secondary peaks at 139 cm⁻¹ and 181 cm⁻¹ are symmetrical about the center of the main peak, while the secondary peaks at 53 cm⁻¹ and 112 cm⁻¹

have no symmetrical relationship.

As the temperature decreases, the intensity of these six TDRS peaks gradually increases from 80 K, followed by a small weakening process near 60 K, which continues until 50 K (see Supplemental Material Fig. S5 for more details). Subsequently, the peak intensity remained basically unchanged until it suddenly increased significantly from 20 K and reached a maximum at 10 K. When the temperature drops below 10 K, the peak intensity gradually decreases with cooling, and the rate of this decrease intensifies as it approaches the superconducting temperature (about 4 K). This trend is illustrated by selecting vibration peaks around 181cm^{-1} as shown in Figure 5(b).

When the temperature drops from 5 K to 1.8 K, the suppression of TDRS peak intensity becomes more pronounced, as shown in Figure 4(c). Compared with the state before superconductivity, each group of TRIS peaks in the superconducting state no longer has central symmetry concerning the main peaks, such as the 139 cm^{-1} and 181 cm^{-1} mentioned above. In the inherently asymmetric 112 cm^{-1} group, compared with the secondary peaks, the main peak is more significantly enhanced (see Supplemental Material Fig. S6 for more details). The significance of these symmetry breaks is consistent with the symmetry breaks observed in STM measurements.

According to previous work [23], 80 K is the starting temperature for the formation of antipolar metallic states. However, the temperature dependence of magnetic susceptibility χ of ATS (see Figure 1(h)) shows a weak magnetic response around 50 K, which is related to the weak decreasing trend of TRDS peaks intensity between 60-50 K. The triple-cube-period CDW is strongest at 10 K, corresponding to the maximum intensity of the TRDS peaks. Subsequently, the temperature continued to decrease until it entered the superconducting state, and CDW was gradually suppressed, but not completely disappeared. The TRDS peaks showed only a relative change in peak intensity throughout the entire process, with almost no significant shift in peak positions, indicating that during the CDW phase transition and superconducting phase transition, there were mainly drastic changes in electronic structure, without accompanying obvious structural phase transitions. This also confirms the characteristic of ATS forming super-strong correlated superconductivity, which is a pure electronic behavior.

III. Discussion

Compared with 9K, the cooling process significantly suppressed TCCDW, especially in LDOS at 300mK where only superatomic Bragg features remained. This once again confirms that TCCDW originates from the translational symmetry breaking of Te...Te CLQB along the a -axis. At 300mK, the inversion symmetry within a triple-cube-period is removed, leading to the transformation of antipolar metallic states into parallel polarization order, which is the result of strong suppression of TCCDW. After the emergence of inversion symmetry breaking, peaks and dips are caused by energy level degeneracy (as shown in Fig. 3 (c)), and more complex stripe-like modulation structures are formed in real space. The dipoles on the UT chain are still retained and form parallel polarized states with the UT chains within the adjacent triple-cube period. The parallel polarized states still interweave with TCCDW. Although the "upper triangular" electronic states on the DT chain no longer switch polarity with bias voltage and lose dipole characteristics, the central inversion symmetry breaking inside each superatom in the chain still exists. The inversion symmetry breaking between UT and DT chains is also reflected in Raman measurements.

The parallel polarized states composed of the original UT chains are robust enough and can coexist with superconductivity. It is rare to directly observe the unexpected coexistence of superconducting states and localized spontaneous polarization states in ATS, a phenomenon currently only observed in doped heterojunction interfaces [31]. In ATS, electrons mainly concentrate on Te...Te CLQB [24], the formation of superconductivity partially suppressed TCCDW and disrupted antipolar metallic states, achieving symmetry breaking in the third dimension.

At 9K, the occupied states of LDOS correspond to the intra-cube states, while the unoccupied states represent the inter-cube states strictly. The electron localization of superatoms is strong, forming charge orders along both the a - and b -axes. At 4K, LDOS displays both intra-cube and inter-cube states in occupied states and unoccupied states. Temperature decreasing causes a reversal in the energy level arrangements of bonding and antibonding molecular orbitals in ATS. Combined with the removal of inversion symmetry at 300mK, it is speculated that these phenomena may be correlated to the BKT topological phase transition [24]. Although the superconductivity of ATS has been determined to be induced by strong electron-electron correlation, further experimental and theoretical investigation is needed for the pairing symmetry of cooper pairs, the real space distribution of superconducting gaps, and whether the chiral or topological superconductivity exists or not. ATS, based on its hierarchical ordered superatomic crystal structure, flexible and controllable CLQB bonding between superatoms, and low symmetry, exhibits remarkably unprecedented quantum states and physical properties, providing a reference for the artificial design and synthesis of more similar new quantum materials.

IV. MATERIALS AND METHODS

Sample preparation

Single crystals of $\text{Au}_6\text{Te}_{12}\text{Se}_8$ (ATS) were grown using the self-flux method, as described in ref [24]. Starting materials with high purity Au powder (99.99%, Sigma Aldrich), Te powder (99.99%, Sigma Aldrich), and Se powder (99.99%, Sigma Aldrich) are stoichiometrically weighted and sealed in an evacuated silica tube in high vacuum and subsequently mounted into a muffle furnace. The furnace was heated up to 850 °C in 24 h and dwelled 48 h. Afterward, the furnace was slowly cooled down to 450 °C in 7 days and then shut down.

STM measurements

STM experiments were performed in a commercial STM (USM-1300- ^3He system with a 16-T magnet) operated in an ultrahigh vacuum (1×10^{-10} mbar), in the Synergic Extreme Condition User Facility, Beijing, China. The energy resolution can reach below 0.26 mV. PtIr alloy tips calibrated on clean Ag(111) surfaces were used for all our STM measurements. The STM topography was obtained in the constant-current mode, and differential conductance (dI/dV) spectra as well as constant bias maps were acquired using a standard lock-in technique at a frequency of 879.9 Hz and under a modulation voltage from 0.2 to 20 mV. The STM measurements were performed at 4.6K and 300mK respectively to obtain the real space electronic structure above and below the ATS superconducting transition temperature ($T_c \sim 2.8$ K). The STM/STS data were processed using Gwyddion and WSxM software.

XRD, SEM, transport, and Raman measurements

The microstructure of ATS was examined using a scanning electron microscope (SEM, SU5000, HITACHI). The chemical composition of ATS was determined by the Energy Dispersive Spectrum (EDS). Powder X-ray diffraction (PXRD) patterns in the *ab*-plane of single crystal ATS are measured using a Rigaku SmartLab 9kw diffractometer with the Cu-K α anode ($\lambda = 1.5408$ Å). The electrical resistivity (ρ), V-I curves, and specific heat capacity (C_p) of ATS were measured through the standard four-wire method and the thermal relaxation method using the physical property measurement system (PPMS-16, Quantum Design). The specific heat below 1.8 K was measured in the physical property measurement system with a He 3 insert. The dc magnetic susceptibility (χ) was characterized using SQUID (MPMS, Quantum Design). The temperature-dependent Raman was measured in the Micro confocal Raman spectrometer (LabRAM HR Evolution, HORIBA) with a continuous-helium-flow optical cryostat.

ACKNOWLEDGMENTS

This project is financially supported by the National Natural Science Foundation of China (Grant Nos. 52302010, 52250308), the Ministry of Science and Technology of China, National Key Research and Development Program "Physical Regulation" Special Project (No. 2023YFA1406500), Major research project of China (No. 92477128), Natural Science Foundation of Inner Mongolia Department of Science and Technology Autonomous Region Youth Fund No. 2024QN01010), High level talent introduction and research funding support of Department of Human Resources and Social Security of Inner Mongolia Autonomous Region (No. 12000-150422225). X. Chen was supported by the National Natural Science Foundation of China (Grant Nos. 52302010). J. G. Guo was supported by the National Natural Science Foundation of China (Grant Nos. 52250308). Z. H. Cheng was supported by the Ministry of Science and Technology of China, National Key Research and Development Program "Physical Regulation" Special Project (No. 2023YFA1406500), a Major research project of China (No. 92477128). S. Y. Xing as supported by the Natural Science Foundation of Inner Mongolia Department of Science and Technology Autonomous Region Youth Fund No. 2024QN01010), High level talent introduction and research funding support of Department of Human Resources and Social Security of Inner Mongolia Autonomous Region (No. 12000-150422225). This work was supported by the Synergetic Extreme Condition User Facility (SECUF, <https://cstr.cn/31123.02.SECUF>).

Z.C., S.X., and X.C. conceived the research project. S.X., Z.W., J.Z., Z.Y., J.Z., and T.Q. performed the STM experiments and analysis of STM data. X.C., T.Y., J.G., X.L.C., H.R., and H.C. grew the single crystals. X.C., T.S., H.R., and M.C. performed transport, SEM, and XRD measurements. X.C., S.X., F.J., H.C., and S.Z. performed Raman measurements. X.L. and W.Z. conducted a theoretical analysis of the experimental data. S.X., X.C., and Z.C. wrote the manuscript with inputs from all authors.

Reference:

-
- [1] Hui Chen, Haitao Yang, Bin Hu, Zhen Zhao, Jie Yuan, Yuqing Xing, Guojian Qian, Zihao Huang, Geng Li, Yuhan Ye *et al.* Roton pair density wave in a strong-coupling kagome superconductor, *Nature* **599**, 222–228 (2021).
- [2] Xilin Feng, Kun Jianga, Ziqiang Wang and Jiangping Hua. Chiral flux phase in the Kagome superconductor AV_3Sb_5 , *Science Bulletin* **66**, 1384–1388 (2021).
- [3] Anuva Aishwarya, Julian May-Mann, Arjun Raghavan, Laimei Nie, Marisa Romanelli, Sheng Ran, Shanta R. Saha, Johnpierre Paglione, Nicholas P. Butch, Eduardo Fradkin *et al.* Magnetic-field-sensitive charge density waves in the superconductor UTe_2 , *Nature* **618**, 928–933 (2023).
- [4] Kota Ishihara, Masaki Roppongi, Masayuki Kobayashi, Kumpei Imamura, Yuta Mizukami, Hironori Sakai, Petr Opletal, Yoshifumi Tokiwa, Yoshinori Haga, Kenichiro Hashimoto *et al.* Chiral superconductivity in UTe_2 probed by anisotropic low-energy excitations, *Nat. Commun.* **14**, 2966 (2023).
- [5] Akito Saka, Yosuke Matsumoto, Ming xuanFu, Takachika Isomae, Masaki Tsujimoto, Eoin O'Farrell, Daisuke Nishio-Hamane and Satoru Nakatsuji, *Interplay between multipolar order and multipole-induced superconductivity in $PrTi_2Al_{20}$* , *Nat. Commun.* **16**, 2114 (2025).
- [6] Brenden R. Ortiz, Samuel M. L. Teicher, Yong Hu, Julia L. Zuo, Paul M. Sarte, Emily C. Schueller, A. M. Milinda Abeykoon, Matthew J. Krogstad, Stephan Rosenkranz, Raymond Osborn *et al.* CsV_3Sb_5 : A Z2 Topological Kagome Metal with a Superconducting Ground State, *Phys. Rev. Lett.* **125**, 247002 (2020).
- [7] Yong Hua, Samuel M. L. Teicher, Brenden R. Ortiz, Yang Luo, Shuting Peng, Linwei Hua, Junzhang Ma, Nicholas C. Plumb, Stephen D. Wilson, Junfeng He *et al.* Topological surface states and flat bands in the kagome superconductor CsV_3Sb_5 , *Sci. Bull.* **67**, 495–500 (2022).
- [8] Mingu Kang, Shiang Fang, Jeong-Kyu Kim^{2,4}, Brenden R. Ortiz, Sae Hee Ryu, Jimin Kim, Jonggyu Yoo, Giorgio Sangiovanni, Domenico Di Sante, Byeong-Gyu Park *et al.* Twofold van Hove singularity and origin of charge order in topological kagome superconductor CsV_3Sb_5 , *Nat. Phys.* **18**, 301–308 (2022).
- [9] P. W. Anderson, Structure of "triplet" superconducting energy gaps, *Phys. Rev. B* **30**, 4000–4002 (1984).
- [10] Mark H. Fischer, Manfred Sigrist, Daniel F. Agterberg, and Youichi Yanase, *Superconductivity and Local Inversion-Symmetry Breaking*, *Annual Rev. of Condensed Matter Phys.* **14**, 153–172 (2023).
- [11] Kwangrae Kim, Hyun-Woo J. Kim, Seunghyeok Ha, Hoon Kim, Jin-Kwang Kim, Jaehwon Kim, Junyoung Kwon, Jihoon Seol, Saegyeol Jung, Changyoung Kim *et al.* Origin of the chiral charge density wave in transition-metal dichalcogenide. *Nat. Phys.* **20**, 1919–1926 (2024).
- [12] Geng Li, Haitao Yang, Peijie Jiang, Cong Wang, Qiuzhen Cheng, Shangjie Tian, Guangyuan Han, Chengmin Shen, Xiao Lin, Hechang Lei *et al.* Chirality locking charge density waves in a chiral crystal, *Nat. Commun.* **13**, 2914 (2022).
- [13] Dongyang Yang, Jingda Wu, Benjamin T. Zhou, Jing Liang, Teri Siu, Kashif Masud Awan, Kenji Watanabe, Takashi Taniguchi, Toshiya Ideue, Teri Siu *et al.* Spontaneous-polarization-induced photovoltaic effect in rhombohedrally stacked MoS_2 , *Nat. Photonics* **16**, 469–474 (2022).
- [14] P. A. Frigeri, D. F. Agterberg, A. Koga, and M. Sigrist, *Superconductivity without Inversion Symmetry: $MnSi$ versus $CePt_3Si$* , *Phys. Rev. Lett.* **92**, 097001 (2004).
- [15] Zhongyi Zhang, Jiangping Hu, Zhenfei Wu, ChenFang, Fu-chun Zhang, Yuxuan Wang and Shengshan Qin, *Topological superconductivity from unconventional band degeneracy with conventional pairing*, *Nat. Commun.* **15**, 7971 (2024).
- [16] K. Semeniuk, M. Pfeiffer, J. F. Landaeta, M. Nicklas, C. Geibel, M. Brando, Khim and E. Hassinger, *Exposing the odd-parity superconductivity in $CeRh_2As_2$ with hydrostatic pressure*, *Phys. Rev. B* **110**, L100504 (2024).
- [17] Yasuhiko Terada, Shoji Yoshida, Atsushi Okubo, Ken Kanazawa, Maojie Xu, Osamu Takeuchi, and Hidemi Shigekawa, *Optical Doping: Active Control of Metal-Insulator Transition in Nanowire*, *Nano Lett.* **8**, 3577–3581 (2008).

-
- [18] Deok Mahn Oh, S. Wippermann, W. G. Schmidt, and Han Woong Yeom, *Oxygen adsorbates on the Si(111)4×1-In metallic atomic wire: Scanning tunneling microscopy and density-functional theory calculations*, *Phys. Rev. B* **90**, 155432 (2014).
- [19] Matthias Batzill, *Mirror twin grain boundaries in molybdenum dichalcogenides*, *J. Phys.: Condens. Matter* **30**, 493001 (2018).
- [20] Ming-Qiang Ren, Shu-Ze Wang, Sha Han, Can-Li Song, Xu-Cun Ma, and Qi-Kun Xue, *Tuning the electronic states and superconductivity in alkali fulleride films*, *AAPPS Bull.* **32**, 1 (2022).
- [21] Chul-Ho Lee, Lian Liu, Christopher Bejger, Ari Turkiewicz, Tatsuo Goko, Carlos J. Arguello, Benjamin A. Frandsen, Sky C. Cheung, Teresa Medina, Timothy J. S. Munsie *et al.* *Ferromagnetic Ordering in Superatomic Solids*, *J. Am. Chem. Soc.* **136**, 16926–16931 (2014).
- [22] V. A. Stoica, N. Laanait, C. Dai, Z. Hong, Y. Yuan, Z. Zhang, S. Lei, M. R. McCarter, A. Yadav, A. R. Damodaran, S. Das, G. A. Stone, J. Karapetrova *et al.* *Optical creation of a supercrystal with three-dimensional nanoscale periodicity*, *Nat. Mater.* **18**, 377–383 (2019).
- [23] Shuya Xing, Linlu Wu, Zilu Wang, Xu Chen, Haining Liu, Shuo Han, Le Lei, Linwei Zhou, Qi Zheng, Li Huang *et al.* *Interweaving Polar Charge Orders in a Layered Metallic Superatomic Crystal*, *Phys. Rev. X* **12**, 041034 (2022).
- [24] J.G. Guo, X. Chen, X.Y. Jia, Q.H. Zhang, N. Liu, H.C. Lei, S.Y. Li, L.Gu, S.F. Jin and X.L. Chen, *Quasi-two-dimensional superconductivity from dimerization of atomically ordered AuTe₂Se_{4/3} cubes*, *Nat. Commun.* **8**, 871 (2017).
- [25] Xu Chen, Ge Fei, Yanpeng Song, Tianping Ying, Dajian Huang, Bingying Pan, Dongliang Yang, Xiaofan Yang, Keyu Chen, Xinhui Zhan *et al.* *Superatomic-Charge-Density-Wave in Cluster-Assembled Au₆Te₁₂Se₈ Superconductors*, *J. Am. Chem. Soc.* **144**, 20915–20922 (2022).
- [26] Yi Liu, Zi-Yi Liu, Jin-Ke Bao, Peng-Tao Yang, Liang-Wen Ji, Si-Qi Wu, Qin-Xin Shen, Jun Luo, Jie Yang, Ji-Yong Liu *et al.* *Superconductivity under pressure in a chromium-based kagome metal*, *Nature* **632**, 1032–1037 (2024).
- [27] Shaohua Liu, Qingchen Duan, Baizhuo Li, Jiaojiao Meng, Wuzhang Yang, Yi Liu, Yi-Qiang Lin, Si-Qi Wu, Jiayi Lu, Jin-Ke Bao *et al.* *Superconductivity and Charge-Density-Wave-Like Transition in Th₂Cu₄As₅*, *J. Am. Chem. Soc.* **146**, 8260–8268 (2024).
- [28] Xu Chen, Jiangang Guo, Chunsheng Gong, Erjian Cheng, Congcong Le, Ning Liu, Tianping Ying, Qinghua Zhang, Jiangping Hu, Shiyan Li *et al.* *Anomalous Dome-like Superconductivity in RE₂(Cu_{1-x}Ni_x)₅As₃O₂ (RE = La, Pr, Nd)*, *iScience* **14**, 171–179 (2019).
- [29] R. C. Dynes, V. Narayanamurti, and J. P. Garno, *Direct Measurement of Quasiparticle-Lifetime Broadening in a Strong-Coupled Superconductor*, *Phys. Rev. Lett.* **41**, 1509–1512 (1978).
- [30] Ying Xing, Zhibin Shao, Jun Ge, Jiawei Luo, Jinhua Wang, Zengwei Zhu, Jun Liu, Yong Wang, Zhiying Zhao, Jiaqiang Yan *et al.* *Surface superconductivity in the type II Weyl semimetal TaIrTe₄*, *Nat. Sci. Rev.* **7**, 579–587 (2020).
- [31] Xian-Kui Wei, Abdur Rehman Jalil, Philipp Rußmann, Yoichi Ando, Detlev Grutzmacher, Stefan Blugel, and Joachim Mayer, *Atomic Diffusion-Induced Polarization and Superconductivity in Topological Insulator Based Heterostructures*, *ACS Nano* **18**, 571–580 (2024).